HHS Public Access

Author manuscript

J Magn Reson. Author manuscript; available in PMC 2023 September 16.

Published in final edited form as:

J Magn Reson. 2023 July ; 352: 107475. doi:10.1016/j.jmr.2023.107475.

Diamond rotors

Natalie C. Golota[a,b,1], **Zachary P. Fredin**[c,1], **Daniel P. Banks**[a,b], **David Preiss**[c], **Salima Bahri**[a,b], **Prashant Patil**[c], **William K. Langford**[c], **Camron L. Blackburn**[c], **Erik Strand**[c], **Brian Michael**[a,b], **Blake Dastrup**[a], **Keith A. Nelson**[a], **Neil Gershenfeld**[c], **Robert Griffin**[a,b,*]

[a]Department of Chemistry, Massachusetts Institute of Technology, Cambridge, MA 02139, USA

[b]Francis Bitter Magnet Laboratory, Massachusetts Institute of Technology, Cambridge, MA 02139, USA

[c]Center for Bits and Atoms, Massachusetts Institute of Technology, Cambridge, MA 02139, USA

Abstract

The resolution of magic angle spinning (MAS) nuclear magnetic resonance (NMR) spectra remains bounded by the spinning frequency, which is limited by the material strength of MAS rotors. Since diamond is capable of withstanding 1.5–2.5x greater MAS frequencies, compared to state-of-the art zirconia, we fabricated rotors from single crystal diamond. When combined with bearings optimized for spinning with helium gas, diamond rotors could achieve the highest MAS frequencies to date. Furthermore, the excellent microwave transmission properties and thermal conductivity of diamond could improve sensitivity enhancements in dynamic nuclear polarization (DNP) experiments. The fabrication protocol we report involves novel laser micromachining and produced rotors that presently spin at $\omega_r/2\pi$ = 111.000 ± 0.004 kHz, with stable spinning up to 124 kHz, using N_2 gas as the driving fluid. We present the first proton-detected $^{13}C/^{15}N$ MAS spectra recorded using diamond rotors, a critical step towards studying currently inaccessible ex-vivo protein samples with MAS NMR. Previously, the high aspect ratio of MAS rotors (~10:1) precluded fabrication of MAS rotors from diamond.

Keywords

Diamond rotors; Laser machining; Magic angle spinning; High frequency spinning

*Corresponding author. rgg@mit.edu (R. Griffin).

[1]These authors contributed equally to this work.

Declaration of Competing Interest

The authors declare that they have no known competing financial interests or personal relationships that could have appeared to influence the work reported in this paper.

RGG, NG, PP, WL, ZF, DPB, CLB, SB, NCG, DP are authors on a pending patent 2021/0146475 A1 and provisional patent 63/385,131 filed by Massachusetts Institute of Technology. DPB is now an employee of Bruker BioSpin. The authors declare no other competing interests.

Data and materials availability

All data needed to evaluate the conclusions in the paper are available in the main text and/or the supplementary materials.

Appendix A. Supplementary material

Supplementary material contains additional information describing the estimation of rotor failure regimes, the laser lathe apparatus, the spin testing apparatus, and the NMR spectral acquisition parameters. Supplementary data to this article can be found online at https://doi.org/10.1016/j.jmr.2023.107475.

1. Introduction

Magic angle spinning (MAS) nuclear magnetic resonance (NMR) is one of the few spectroscopic techniques that can determine molecular structures at atomic resolution while probing molecular dynamics in insoluble, non-crystalline biomolecules and materials [1,2]. Accordingly, over the past two decades, MAS, together with dipole recoupling experiments [3], has evolved into a critical tool for structural biology research in systems such as amyloid fibrils [4-8] membrane proteins [9-11], macromolecular viral assemblies [12,13] and in a variety of materials science problems [14-16]. Despite these successful studies, many of the most pressing and complex biomedical and materials science challenges remain inaccessible due to limited resolution, inherently poor sensitivity, and the requirements for copious isotopically enriched samples.

To address these limitations in solids, several decades of development have led to the advent of sophisticated MAS stators and rotors, and a progressively miniaturized series of yttria-stabilized zirconia (YSZ) cylindrical and more recently spherical rotors [17-21]. While MAS rotors have been fabricated using a variety of materials — silicon nitride, sapphire, Delrin® and MACOR® — only YSZ has been employed to date in the fabrication of commercially available rotors less than 3 mm in outer diameter. With commercially available 0.7 mm YSZ rotors and N_2 gas as the driving fluid, MAS frequencies up to 111 kHz are routinely achieved. More recently prototype 0.4 mm and 0.5 mm YSZ rotors were reported to spin at $\omega_r/2\pi$ = 150 to 200 kHz MAS [22,23], again using N_2. At present the spinning frequencies are limited by the speed of sound in N_2. However, the improved resolution and sensitivity from spinning frequencies >100 kHz have enabled important insights into the study of samples ranging from amyloid fibrils to membrane proteins [24-26]. Despite these significant advances, the achievable proton resolution under MAS restricts ubiquitous adoption of proton detection in the solid-state, as is performed in solution NMR. We note in some samples, the inhomogeneous linewidth due to sample specific parameters may dominate over the homogenous linewidth and will not be modulated by faster MAS frequencies. Despite this, in many fully protonated protein samples, it has been shown that the homogeneous linewidth due to the dense dipolar coupled proton network dominates the observed linewidth and would benefit from increased MAS frequencies. Recognizing this limitation, several groups have calculated the theoretical MAS frequency required to yield solution like linewidths and coherence lifetimes in solids to be ~ 300 kHz and in many cases up to 1 MHz (18–60 × 10^6 RPM) [27-29].

In addition to proton-detected MAS methods, dynamic nuclear polarization (DNP) can be used to enhance the sensitivity of solid-state NMR. DNP uses microwave irradiation to transfer the high spin polarization of electrons to nuclear spins at cryogenic temperatures (typically ~ 100 K), offering a theoretical maximum enhancement of ~ 660 relative to conventional NMR [30,31]. This has stimulated significant developments with gyrotron microwave sources and low temperature MAS probes that have enabled DNP on biomolecules in frozen solution with enhancements routinely yielding ~ 50–100 [32-34]. However, at the high magnetic fields (>16.4 T) required for improved spectral resolution, typical CW DNP mechanisms become less efficient. Consequently, the continued development of high field DNP methods is focused on improving (a) polarizing agent

efficiency, (b) microwave coupling efficiency into the rotor, (c) the achievable sample temperature, with lower temperatures yielding higher enhancements, (d) instrumentation for time domain DNP experiments and (e) the achievable MAS frequency at 100 K [35-44].

The continued expansion of MAS NMR to the most biomedically relevant systems likely requires realizing spinning frequencies >300 kHz coupled with improved efficiency during DNP experiments. Current MAS NMR rotor technology has relied solely on decreasing the rotor diameter to achieve higher spinning frequencies, with a resulting decrease in sample volume up to the cube of the rotor radius. However, rotor diameters and associated spinning components are approaching fabrication limitations while the MAS frequency remains insufficient. Thus, without introducing new rotor materials used to fabricate MAS rotors, the required higher MAS frequencies are increasingly difficult to achieve.

The study of currently inaccessible ex-vivo protein samples using MAS NMR motivated our development of novel laser micromachining methods. These applications require the combination of high spinning frequencies, $\omega_r/2\pi$ > 100 kHz, with large sensitivity enhancements from DNP at high magnetic fields. In particular, it is critical to employ a new rotor material and associated fabrication methodology that will enable MAS in the 150–300 kHz regime. The desirable properties of the material should include high strength, high thermal conductivity, and low THz absorption material, and, as illustrated in Fig. 1 the ideal material to simultaneously satisfy these three criteria is single crystal diamond. Additional data relevant to this point is available in the Supporting Information, Figure S1. Diamond's cubic crystal structure provides exceptionally high atomic bond strengths, making it one of the strongest materials available. However, the high strength of diamond also prohibits application of traditional mechanical drilling or abrasive grinding methods. While laser machining is utilized to fabricate diamond micro-structures, the required ~ 10:1 aspect ratio (referring to the ratio between the length and inner diameter of the rotor), μm tolerances and near zero internal taper of MAS rotors were thought to be unattainable using available laser machining strategies. As such, there were no commercially available methods of fabricating diamond rotors.

Herein we describe a novel laser micromachining strategy using dual-sided axial ablation to fabricate diamond rotors with less than 0.05° of internal taper while maintaining micron tolerances. We quantify spinning stability at $\omega_r/2\pi$ = 111 kHz with a standard deviation in spinning frequency of less than 4 Hz (0.004%), further demonstrating the success of the machining strategy. Finally, we present the initial ^{1}H detected MAS NMR spectra obtained using diamond rotors. These results highlight the feasibility and potential dramatic change that continued development of such technology can bring to the field of solid-state NMR.

2. Experimental

2.1. Rotor fabrication

Rotors were fabricated using an Oxford Lasers (Didcot, Oxfordshire, UK) A-series laser micromachining system equipped with a Q-switched 532 nm diode-pumped Nd:YAG laser with a spot size of 13–14 μm. The pulse duration was ~ 20 ns at a repetition rate of 5 kHz. Single crystal high pressure high temperature (HPHT) type Ib diamond was purchased

from Element6 (Didcot, Oxfordshire, UK) for ~ $20/mm^3. All machining operations were aligned to the 100 (4 point) crystal axis to avoid the (111) diamond cleavage plane. A lab-fabricated precision lathe apparatus was used for all machining operations and relied upon a Thorlabs (Newton, NJ, USA) DDR100 direct drive rotary stage to achieve rotational frequency of 2.76 Hz (166 RPM) during both inner and outer diameter machining steps. The diamond was secured using a flexural clamp fabricated from 17–4 stainless steel and was mechanically flipped for a second axial machining step to reduce inner diameter taper. Alignment was maintained in this process through use of a fabricated Kelvin-style magnetic kinematic coupling system (Figure S2). Typical laser fluences employed ranged from 300 J/cm^2 to 770 J/cm^2. A complete description of the fabrication process is given in Figure S3. Following fabrication, the rotors were subjected to 24 h of heat treatment at 600 °C in air using a tabletop oven to remove the graphite and amorphous carbon film formed and deposited on the diamond during machining.

2.2. Rotor characterization

Immediately following machining, graphite coated machined surfaces were characterized using a Hitachi scanning electron microscope FlexSEM1000 (Tokyo, Japan). Inner diameter tapers were measured using a Nikon Metrology XT H 160 (Micro Computed-Tomography) scanner (Tring, UK) at 3 μm voxel resolution. CT reconstruction was performed using CT Pro3D XT 5.4 software (Nikon Metrology, Tring, UK) and visualized using VGStudio by Volume Graphics Inc. (Charlotte, NC, USA). Rotor inner and outer diameters were characterized using a Keyence (Osaka, Japan) TM-X5006 telecentric measurement system with ± 0.2 μm measurement positional accuracy. A detailed description of rotor measurements is given in Section S3.

2.3. Raman analysis

Single crystal HPHT diamond was analyzed without modification, in addition to machined samples pre- and post-heat treatment. Highly ordered pyrolytic graphite (HOPG) ZYB quality was purchased and used without modification from Ted Pella (Redding, CA, USA) as a graphite standard. Raman analysis was performed using a Renishaw Invia Reflex spectrometer equipped with a confocal microscope. Raman excitation was performed using a 532 nm laser. Raman shifts were calibrated against a silicon standard and data was processed using Renishaw's WiRE™ software.

2.4. THz transmission measurements

Terahertz transmission spectra were collected using a standard terahertz time-domain spectroscopy (THz-TDS)[49]. Broadband THz radiation was generated by optical rectification in a 1 mm thick ZnTe crystal using the 1 mJ, 100 fs output of an Astrella Ti: Sapphire regenerative amplifier (Coherent Inc, Santa Clara, CA USA) operating at a repetition rate of 1 kHz and with a center wavelength of 800 nm. The THz beam was focused onto the sample (beam waist ~ 2 mm) at normal incidence, and then collected and refocused onto a 2 mm thick ZnTe crystal for electro-optical detection using three paraboloid mirrors after sample transmission. Sample thicknesses were 1.93 mm, 1.17 mm, and 6.37 mm for zirconia, diamond, and sapphire, respectively. 10% of the amplified laser output was split off prior to THz generation, time-delayed, and recombined with the THz

beam at the detection crystal. Time-domain traces of the THz electric field were obtained by time delaying the THz and 800 nm probe pulses with respect to each other in a stepwise fashion. In this process, the instantaneous THz electric field at each time-step is encoded onto the polarization state of the probe pulse, which is then read out using a typical balanced detection scheme. THz transmission spectra were then obtained by computing the fast Fourier transform of the time-domain THz traces collected with and without the sample in place. The refractive index, surface reflections, and absorption coefficient were used to compute the absorption and reflection coefficients, A and R (Figure S1). These were then used to compute the percent transmission for a 1 mm sample thickness of each material using the equation T = 1-A-R.

2.5. MAS stability testing

Diamond rotors were machined to accommodate Bruker BioSpin (Billerica, MA, USA) Vespel drive tips and end caps. For MAS stability tests, rotors were packed with potassium bromide powder (KBr) purchased from Millipore-Sigma (Burlington, MA). Spinning frequency control was achieved using dry N_2 spinning gas, a MAS 3 Controller (Bruker BioSpin, Billerica MA, USA), and a 0.7 mm test stand system (Bruker BioSpin, Billerica, MA USA) (Figure S9). The MAS frequency was recorded at 1 s intervals using a Rigol oscilloscope (Suzhou, China) DS1104Z oscilloscope and logged using a Python script. The spinning frequency data was analyzed using Matlab (Mathworks, Natick MA). A 0.7 mm YSZ rotor was used as a standard in MAS stability measurement and was purchased from Bruker BioSpin. 1.3 mm YSZ rotors used in failure testing were purchased from Bruker and O'Keefe Ceramics (Woodland Park, CO USA), packed with KBr, and fitted with end caps and drive tips which were purchased from Bruker BioSpin.

2.6. NMR spectroscopy

A diamond rotor was packed with a 1:1 mixture of (U-^{13}C,^{15}N)-N-Formyl-methionyl-leucyl-phenylalanine-OH ((U-^{13}C,^{15}N)-N-*f*-MLF-OH) previously packed into a larger MAS rotor and zirconia powder (Sigma Aldrich, St. Louis MO). All spectra were acquired at a static field of 18.8 T (800 MHz ^{1}H) with a three channel (HCN) 0.7 mm Bruker MAS probe. The sample was spun at $\omega_r/2\pi$ = 111 kHz using a MAS 3 controller. The 90° pulse durations were 1.875 μs, 3 μs, and 3 μs for ^{1}H, ^{13}C, and ^{15}N, respectively. Dipolar based CP-HSQC spectra were recorded using the pulse sequence previously described [50]. $^1H \rightarrow {}^{13}C$ forward cross polarization (CP) was achieved with a contact time of 2 ms while the ^{1}H RF-field amplitude was ramped from 142 kHz to 158 kHz and the carbon RF field was constant at 36 kHz. $^{13}C \rightarrow {}^1H$ reverse CP was achieved using a contact time of 1.2 ms while the proton RF field amplitude was ramped from 158 kHz to 142 kHz while the ^{13}C RF amplitude was constant at 45 kHz. $^1H \rightarrow {}^{15}N$ forward CP was achieved with a contact time of 1.5 ms while the proton RF amplitude was ramped from 140 kHz to 156 kHz and the ^{15}N RF amplitude was constant at 28 kHz. The $^{15}N \rightarrow {}^1H$ reverse CP was achieved with a 1.2 ms contact time during which the ^{1}H RF field was ramped from 156 kHz to 140 kHz while the ^{15}N RF amplitude was constant at 40 kHz. During both CP-HSQC experiments, swept-low power TPPM at an RF field amplitude of 22.6 kHz was used for proton decoupling during t_1 and WALTZ-16 was applied to ^{13}C or ^{15}N at RF field strengths of 10 kHz [51,52]. Water suppression was achieved through the MIS-SISSIPPI pulse sequence without homospoil

gradients [53], using a 23 kHz RF field and 200 ms pulse duration. Spectra were apodised using 60° shifted squared sine bells and zero filled to at least twice the number of points in the indirect dimension. Additional acquisition parameters are given in Table S2.

3. Results and discussion

To address current limits in MAS instrumentation, and thus applications of MAS NMR, we developed laser micromachining methods to fabricate diamond rotors. Prior to this work, it was predicted that the combined high aspect ratio, micron tolerances and near zero required internal taper angle could not be achieved in diamond. However, we demonstrated a dual-sided axial machining strategy that enabled fabrication of diamond rotors. During nanosecond laser machining of diamond, thermal energy is absorbed by imperfections in the diamond crystal lattice, resulting in a phase transformation from diamond to graphite. At radiation levels beyond the threshold fluence of diamond, graphite is largely vaporized and expelled from the inner diameter of the hole. However, during this process, the laser beam becomes partially attenuated by the formation of a plasma, effectively reducing the depth of hole that can be obtained in diamond. Fluences at least twenty-five times the ablation threshold for diamond combined with dual-sided axial machining allowed sufficient radiation incident to the diamond, enabling the fabrication of ~ 5 mm deep holes in diamond with ~ 0.5 mm diameters as illustrated in Fig. 2.

To quantify the geometric dimensions and tolerances achieved during laser micromachining, we employed a variety of methods including SEM, microCT and optical telecentric measurement. The dimensions for several commercial zirconia rotors and diamond NMR rotors fabricated in-house are tabulated in the supporting information, (Table S1). Typical measured outer diameters and rotor-to-rotor tolerances are 695 ± 5 μm, as determined using a non-contact optical telecentric measurement system with a published accuracy of ± 0.2 μm. With this method, we were able to achieve typical internal tapers of less than ~ 0.05° over 4.6 mm, as determined by analysis of SEM data (Fig. 3) and verified by microCT (Fig. 2D). The resulting rotors produced using mechanical re-orientation (Figure S2) demonstrated an inner and outer diameter concentricity error of less than 13 μm for all rotors, as shown in the SEM measurements (Fig. 3).

The total fabrication time per rotor, which is mostly automated, is currently ~ 6–10 h, with the potential for optimization to further reduce the fabrication time. The reproducibility of the fabrication scheme used to date is highly dependent on the structural integrity of the flexural clamping mechanism used to hold the rotor during fabrication, illustrated in the supplemental information, along with operator technique and careful alignment of the machining apparatus. These shortcomings can be further improved by changing the machining methodology to reduce the need for manual manipulation of partially machined rotors. Despite this, our current strategy for fabricating diamond rotors is uniquely suited to continued miniaturization of MAS components, whereas conventional ceramic drilling technologies are already approaching feasibility limitations. For further details on the machining process, we refer the reader to the supplementary information.

Raman spectra shown in Fig. 4 was used to confirm the laser ablation mechanism previously presented in the literature [54-57]. We confirmed the presence of the single, narrow resonance associated with single crystal diamond (Fig. 4A) in the starting, un-machined material at ~ 1332 cm^{-1} (Fig. 4D), in accordance with literature values [58]. Following laser ablation (Fig. 4B), a resonance at ~ 1585 cm^{-1} was observed, characteristic of the G band of graphite [59]. In the machined sample, we observed this band had broadened relative to a highly orientated pyrolytic graphite (HOPG) standard sample (Fig. 4E). Therefore, we conclude amorphous carbon species are formed as indicated by the broadening of both resonances in addition to graphite formation. Finally, we note the reduced intensity of the graphite signal relative to the diamond signal in the machined sample. This supports optical telecentric measurements taken before and after heat treatment indicating the layer of graphite formed is on the order of 1–2 μm thick.

For use in DNP and conventional NMR applications, the electrically conductive graphite species must be entirely removed from the rotor prior to use in experiments. The surface graphite could prohibit efficient transmission of microwaves into the rotor for DNP and serve as a potential source of electrical arcing to the transmit and receive coil. To remove the accumulated graphite, a high temperature oxidative step was employed at 600 °C for 24 h [60,61]. Following heat treatment, the Raman analysis was repeated, and a signal from graphite or other sp^2 carbon species was absent (Fig. 4C and 4F). Overall, Raman spectroscopy confirmed the ablation mechanism and importantly verified the absence of graphite at the end of rotor processing.

All 0.7 mm rotors were packed with potassium bromide ($\rho_{KBr} = 2.75 g/cm^3$) and spun to 111 kHz manually using a test stand with MAS 3 controller supplied by Bruker. As illustrated in Fig. 5, the standard deviation in spinning stability over the course of one hour at 111 kHz was determined to be 3.13 Hz and 4.04 Hz for each of the two diamond rotors we tested (Fig. 5B, C, E, F). The standard deviation in spinning stability over one hour was also measured for a zirconia rotor at 111 kHz and was determined to be 4.43 Hz (Fig. 5A, D). We note here the spinning stability is impacted by both the rotor-bearing interaction, which is modulated by rotor mass imbalance, and the stability of the drive and bearing gas regulation. The measured stability of the MAS 3 controller used for these experiments was 2696 ± 2.14 mBar and 4112 ± 5.35 mBar, for bearing and drive gas, respectively. Importantly, using diamond rotors results in a decrease in the force exerted on the rotor by ~ 40%, afforded by the reduction in rotor density when using diamond (3.5 g/cm^3) relative to YSZ (~6.0 g/cm^3).

In Fig. 6 we show ^{1}H-detected ^{13}C and ^{15}N MAS NMR spectra of N-formyl-methionyl-leucyl-phenylalaninol (N-*f*-MLF-OH) recorded using a diamond rotor for a proof of concept set of experiments at $\omega_r/2\pi$ = 111 kHz. Likely due to the minor remaining concentricity errors discussed previously, the spin-up profile of the diamond rotors is non-linear (Figure S11); we attribute this behavior to excitation of translational and whirl resonance conditions between 2 and 20 kHz [62]. To reduce risk to the NMR probe while increasing $\omega_r/2\pi$, the N-*f*-MLF-OH powder was mixed in a 1:1 ratio with YSZ powder, which reduced the effective concentricity error, lowering the translational and whirl resonance conditions. This improved the linearity of response to drive gas and ensured the NMR probe was not damaged during these initial experiments. However, the rotors are sufficiently concentric

and balanced to achieve highly stable rotation at $\omega_r/2\pi > 111$ kHz (6.6×10^6 RPM) with lower density samples. The dipolar based (H)NH and (H)CH heteronuclear correlation experiments were recorded without electric arcing, confirming the absence of electrically conductive graphite. Additionally, the spectra obtained were free of any ^{13}C background signal from the diamond rotor itself. Recall, the ^{13}C occurs at natural abundance, and the ^{13}C T_{1n} diamond is long. Of course, the use of cross polarization transfer steps insured excitation of only ^{15}N or ^{13}C adjacent to ^{1}H, preventing detection of ^{13}C from the diamond rotor itself. The acquisition of proton-detected heteronuclear correlation spectra in Fig. 6 demonstrates the utility of diamond rotors for use in NMR and their compatibility with standard, commercially available instrumentation.

Resolution in MAS NMR experiments remains limited by the accessible spinning frequency. To date, rotor outer diameters have been continuously decreased to access higher MAS frequencies using YSZ. Despite these efforts, the current maximum MAS frequency achievable is 200 kHz, only 20% of the upper bound of the MAS frequency theoretically thought to be necessary to achieve solution-like resolution in complex, solid state biomolecules. At present, the highest MAS frequencies can be achieved using 0.4 mm rotors, which approach the practical limit of conventional ceramic machining practices.

The maximum achievable MAS frequency is ultimately determined by three factors: (1) the speed of sound of the gas used in the air bearings and gas turbine, (2) the structural integrity of the rotor material used, and (3) the efficiency of the turbine and air bearings. Significant rotor turbulence and reduced drive efficiency is expected as the circumferential frequency of the rotor approaches the speed of sound for a given spinning gas [63]. The maximum MAS frequency of a rotating cylinder is given by the rotor's circumferential frequency of $v/2\pi r$, where v is speed of sound of the gas used and $2\pi r$ is the rotor outer diameter. For a 0.7 mm diameter rotor and nitrogen gas, the maximum circumferential frequency is 161 kHz or a surface velocity of 354 m/s. In practice, MAS rotors typically operate at a maximum ~ 80% of the speed of sound in N_2 or air (~125 kHz) due to frictional losses in the air bearings [63]. Using nitrogen gas, we achieved maximum MAS frequencies of 123 kHz, which has a corresponding surface speed of 264 m/s, or roughly 75% the speed of sound. 0.7 mm YSZ rotors are rated to 111 kHz, or 68% the speed of sound.

To exceed these frequencies, helium gas can in principle be used to access a ~ 3 times improvement in spinning frequency afforded by a ~ 3 times increase in the speed of sound of helium gas relative to nitrogen, (Fig. 1A) [45]. To date, helium has mainly been used in solid-state NMR to realize low temperature experiments for improved sensitivity under DNP, notably without observation of electrical arcing [17,64-69]. However, the use of helium to achieve higher spinning frequencies at room temperature has been restricted to use with large rotors due to challenges with the stability of current air bearing designs which are not sized for use with helium lubricant [20,70]. Recently, significant efforts in the optimization of air bearings for use with helium gas and 0.4 mm zirconia rotors resulted in a maximum spinning frequency of only 18 kHz, compared to 110 kHz in air [70]. The maximum MAS frequency we achieved with a 0.7 mm rotor and 100% helium gas was 80 kHz. When tested, the rotor stability was extremely poor and changes in drive or bearing pressures by less than 10–20 mbar resulted in fluctuations in the MAS frequency of several kHz or could lead

to rotor crash. With a 70:30 volumetric mixture of helium: nitrogen gas, diamond rotors were spun to 124 kHz but could not be increased past this point (Figure S10). At 124 kHz the significant rotor instability led to a diamond rotor crash, however, the rotor was recovered intact and without damage. The same rotor was spun to ~ 123 kHz with nitrogen gas and did not display this instability, in agreement with past observations using helium gas. As shown in Figure S12, using He gas as the driving fluid, we found the initiation of MAS is nontrivial and generally unreproducible with 0.7 mm rotors. 1.3 mm YSZ rotors achieved 88–89 kHz using 100% helium gas when packed with KBr, however, this required considerable optimization of the bearing and drive pressures.

The non-trivial application of helium gas to rotors less than 1.3 mm in diameter is likely due to insufficient bearing stiffness when helium gas is used in bearings design for air or nitrogen. Thus, access to higher MAS frequencies using helium requires fabricating bearings designed for helium gas by varying both the radial air gap and nozzle diameter to increase radial bearing stiffness. Overall, our result of $\omega_r/2\pi$ = 124 kHz using a mixture of He and N_2 represents to our knowledge the highest MAS frequency achieved with helium. Prior to the fabrication of diamond rotors, the insufficient material strength of YSZ did not make the considerable investment into helium optimized bearings worthwhile. However, with the demonstration of diamond rotor technology and in-house diamond machining capabilities, helium optimized bearings have become a necessary and realistic research objective.

As the failure point of diamond rotors could not be obtained experimentally, we evaluated three models associated with rotor failure. Previous literature describing rotor failure is based on the tensile strength or the elastic modulus in determining hoop stress and bending mode limited frequencies, respectively [20,71,72]. In practice, failure of MAS rotors fabricated from brittle materials is more likely due to surface defects (flaws and cracks) serving as a stress concentration point from which failure is initiated [73-75]. These defects reduce the effective toughness of the material below its theoretical maximum with corresponding underperformance in MAS. In general, given comparable surface defect concentrations, a material with a higher fracture toughness resists crack propagation and performs more closely to its theoretical strength and toughness than a material with a low fracture toughness. The relative performance of MAS rotor materials is properly predicted using basic fracture mechanics, given in terms of relative angular frequency to that of YSZ in Fig. 7 and considers the fracture toughness, density, and Poisson's ratio for each material [76]. For further details on this calculation, we refer the reader to the supporting information. The fracture toughness of YSZ can vary as a function of mol % yttria stabilization with typical values between 3 and 8 MPa•$m^{1/2}$[77-79]. For the 1.3 mm YSZ rotors tested in this paper and stabilized with 5 mol % yttria the fracture toughness is 7 MPa•$m^{1/2}$. We note that specially engineered zirconia has reached fracture toughness up to 15 MPa•$m^{1/2}$[80]. For further comparison, we included silicon nitride which has been used in larger MAS rotors and typically achieve higher MAS frequencies than YSZ rotors. The fracture toughness is comparable to YSZ, but the reduced density accounts for improved performance over YSZ. Finally, fracture mechanics properly predicts that sapphire has the lowest anticipated MAS performance due to its low fracture toughness.

Basic fracture mechanics were applied to determine the theoretical performance of nitrogen doped single crystal chemical vapor deposition (CVD) diamond, type Ib HPHT diamond (used in this work), silicon nitride, type IIa natural diamond, and sapphire all relative to yttria stabilized zirconia.

Diamond offers the advantage of improved fracture toughness and reduced density relative to YSZ. HPHT type Ib diamond has a fracture toughness in the range of 10 ± 2 MPa•$m^{1/2}$, while nitrogen and/or boron doping of CVD diamond can increase the fracture toughness beyond 34 MPa•$m^{1/2}$[81]. Type IIa natural diamond has a lower fracture toughness between 4 and 5 MPa•$m,^{1/2}$ but the reduced density results in comparable predicted performance, relative to YSZ, using fracture mechanics. A forthcoming publication demonstrates that nanosecond laser machining of diamond does not significantly alter the crystal lattice or introduce strain that would result high concentrations of surface defects leading to reduced performance in MAS. Finally, on the basis of hoop stress and bending mode failure regimes, the high tensile strength of diamond and high elastic modulus offer superior performance over other MAS rotor materials, as described in the supplemental information. Across the three analyses, we estimate an increase in achievable MAS frequency by ~ 1.5–2.5 times with diamond rotors.

We emphasize the approximate nature of these calculations, rotor failure can occur below the estimated frequencies due to the role of surface defects, sample packing, turbine imperfections, gas delivery failures and user error. For a precise model of rotor failure, complex fracture mechanics based finite element analysis or machine learning may be employed considering surface defects, fracture toughness, and yield strength[75,82]. Finally, efforts into measuring these parameters of MAS rotors could be worthwhile, though previously non-trivial given the small sample sizes[83]. Ultimately, the only way to determine the failure regime of diamond rotors is through extensive failure testing with helium gas.

Beyond the improvement in accessible MAS frequency, diamond rotors offer significant advantages for both ambient MAS NMR and DNP NMR. The higher thermal conductivity and improved microwave transmission properties are expected to result in improved sample cooling and stability larger DNP enhancements compared to traditional zirconia rotors. The improved thermal conductivity of diamond is expected to dissipate heat resulting more efficiently from microwave irradiation or frictional heating at fast MAS. More rapid and effective dissipation of heat reduces cooling demands for MAS NMR of biological samples at room temperature, in addition to DNP conditions. A potentially lower sample temperature afforded by diamond rotors with more effective sample cooling under DNP is expected to result in increased enhancements for the same microwave irradiation power in a zirconia rotor. As shown in Fig. 1C, the THz transmission spectra of diamond and sapphire are relatively comparable, with diamond having a slight advantage. However, as shown in the supplementary material, diamond has lower surface reflection afforded by the low refractive index. In contrast, sapphire has a relatively high transmission across the THz regime, but the increased refractive index results in higher surface reflections. Overall, zirconia offers poor THz transmission in addition to high surface reflections. The high transparency of diamond coupled with low surface reflections makes diamond an optimal material for MAS DNP

rotors at high fields. The experimental validation of diamond rotors under DNP is the subject of future work.

4. Conclusion

Diamond rotors offer the most promising technology to achieve solution-like resolution and coherence lifetimes in the solid-state. We have presented a new and novel laser machining method using dual-sided axial ablation to fabricate 0.7 mm diamond rotors, spun the rotors to $\omega_r/2\pi$ = 123 kHz using N_2 gas, and used the rotors to record ^{1}H detected MAS spectra at 18.8 T. Importantly, future developments and applications of this work can enable improved resolution and sensitivity in NMR and DNP enhanced NMR. In particular, diamond rotors, in addition to drive tips and end caps fabricated from diamond and helium bearings optimized for diamond rotors, should offer the ability to reach higher MAS frequencies. Along with improved microwave transmission and thermal conductivity diamond rotors offer a route toward performing high resolution ^{1}H detected DNP for unprecedented sensitivity and resolution of currently inaccessible biomolecules.

Supplementary Material

Refer to Web version on PubMed Central for supplementary material.

Acknowledgments

The authors thank Bruker BioSpin for support of the project including the supplied MAS 3 and 0.7-mm test stand. We additionally acknowledge the project support and helpful conversations from Armin Purea, Rico Simmler, Sebastian Wegner, Jochem Struppe, and Albert Donkoh. We thank Christos Anthanasiou for assistance regarding fracture mechanics. We gratefully acknowledge helpful conversations and technical support from Edward Saliba, Lauren Schafer, Sam Calish, Michael Mullins and Stephen Thomson. We thank Jack Forman for assistance in acquiring high resolution images of diamond rotors and stages of the fabrication process.

Finally, we acknowledge the assistance of Dr. Charles Settens at the MIT Materials Research. Laboratory for access to and assistance with the Raman spectrometer used in this work.

Funding

This project is funded by the National Institutes of Health under grants GM139055 (NG), and GM132997, GM132079 and AG058504 (RGG). Additional support was provided by the CBA Consortia fund. BD and KAN acknowledge support from the U.S. Department of Energy, Office of Basic Energy Sciences under award No. DE-SC0019126. NCG is supported by the National Science Foundation Graduate Research Fellowship under Grant No. 1744302. This work made use of the MRSEDC Shared Experimental Facilities at MIT, supported by the National Science Foundation under award number DMR-1419807.

Data availability

No data was used for the research described in the article.

References

[1]. Bonaccorsi M, Le Marchand T, Pintacuda G, Protein structural dynamics by Magic-Angle Spinning NMR, Curr. Opin. Struct. Biol 70 (2021) 34–43. [PubMed: 33915352]

[2]. Berruyer P, Emsley L, Lesage A, DNP in materials science: touching the surface, eMagRes (2018) 93–104.

[3]. Bennett AE, Griffin RG, Vega S, Recoupling of Homo- and Heteronuclear Dipolar Interactions in Rotating Solids, in: Blümich B (Ed.), Solid-State NMR IV Methods and Applications of Solid-State NMR, Springer, Berlin Heidelberg, Berlin, Heidelberg, 1994, pp. 1–77.

[4]. Colvin MT, Silvers R, Ni QZ, Can TV, Sergeyev I, Rosay M, Donovan KJ, Michael B, Wall J, Linse S, Griffin RG, Atomic resolution structure of monomorphic Aβ42 Amyloid Fibrils, J. Am. Chem. Soc 138 (2016) 9663–9674. [PubMed: 27355699]

[5]. Lu J-X, Qiang W, Yau W-M, Schwieters CD, Meredith SC, Tycko R, Molecular structure of β-Amyloid Fibrils in Alzheimer's disease brain tissue, Cell 154 (2013) 1257–1268. [PubMed: 24034249]

[6]. Reif B, Ashbrook SE, Emsley L, Hong M, Solid-state NMR spectroscopy, Nat. Rev. Methods Primers 1 (2021) 2. [PubMed: 34368784]

[7]. Wälti MA, Ravotti F, Arai H, Glabe CG, Wall JS, Böckmann A, Güntert P, Meier BH, Riek R, Atomic-resolution structure of a disease-relevant Aβ(1–42) amyloid fibril, Proc. Natl. Acad. Sci 113 (2016) E4976–E4984. [PubMed: 27469165]

[8]. Schütz AK, Vagt T, Huber M, Ovchinnikova OY, Cadalbert R, Wall J, Güntert P, Böckmann A, Glockshuber R, Meier BH, Atomic-resolution three-dimensional structure of Amyloid β Fibrils bearing the Osaka mutation, Angew. Chem. Int. Ed 54 (2015) 331–335.

[9]. Eddy MT, Yu T-Y, Wagner G, Griffin RG, Structural characterization of the human membrane protein VDAC2 in lipid bilayers by MAS NMR, J. Biomol. NMR 73 (2019) 451–460. [PubMed: 31407201]

[10]. Mandala VS, Williams JK, Hong M, Structure and dynamics of membrane proteins from solid-state NMR, Annu. Rev. Biophys 47 (2018) 201–222. [PubMed: 29498890]

[11]. Wang S, Ladizhansky V, Recent advances in magic angle spinning solid state NMR of membrane proteins, Prog. Nucl. Magn. Reson. Spectrosc 82 (2014) 1–26. [PubMed: 25444696]

[12]. Lecoq L, Fogeron M-L, Meier BH, Nassal M, Böckmann A, Solid-state NMR for studying the structure and dynamics of viral assemblies, Viruses 12 (2020) 1069. [PubMed: 32987909]

[13]. Porat-Dahlerbruch G, Goldbourt A, Polenova T, Virus structures and dynamics by magic-angle spinning NMR, Ann. Rev. Virol 8 (2021) 219–237. [PubMed: 34586870]

[14]. Berruyer P, Lelli M, Conley MP, Silverio DL, Widdifield CM, Siddiqi G, Gajan D, Lesage A, Copéret C, Emsley L, Three-dimensional structure determination of surface sites, J. Am. Chem. Soc 139 (2017) 849–855. [PubMed: 27997167]

[15]. Kong X, Deng H, Yan F, Kim J, Swisher JA, Smit B, Yaghi OM, Reimer JA, Mapping of functional groups in metal-organic frameworks, Science 341 (2013) 882–885. [PubMed: 23887875]

[16]. Pecher O, Carretero-González J, Griffith KJ, Grey CP, Materials' methods: NMR in battery research, Chem. Mater 29 (2017) 213–242.

[17]. Andrew ER, Farnell LF, Firth M, Gledhill TD, Roberts I, High-speed rotors for nuclear magnetic resonance studies on solids, J. Magn. Reson 1 (1969) (1969) 27–34.

[18]. Beams JW, An apparatus for obtaining high speeds of rotation, Rev. Sci. Instrum 1 (1930) 667–671.

[19]. Chen P, Albert BJ, Gao C, Alaniva N, Price LE, Scott FJ, Saliba EP, Sesti EL, Judge PT, Fisher EW, Barnes AB, Magic angle spinning spheres, Sci. Adv 4 (2018) eaau1540. [PubMed: 30255153]

[20]. Doty FD, Ellis PD, Design of high speed cylindrical NMR sample spinners, Rev. Sci. Instrum 52 (1981) 1868–1875.

[21]. Schledorn M, Malär AA, Torosyan A, Penzel S, Klose D, Oss A, Org M-L, Wang S, Lecoq L, Cadalbert R, Samoson A, Böckmann A, Meier BH, Protein NMR spectroscopy at 150 kHz magic-angle spinning continues to improve resolution and mass sensitivity, Chembiochem 21 (2020) 2540–2548. [PubMed: 32501630]

[22]. BioSpin B, 160 kHz Ultra-fast MAS, International Conference on Magnetic Resonance in Biological Systems, Boston, MA, USA, 2022.

[23]. Samoson A, 0.2 MHz MAS, experimental nuclear magnetic resonance conference, Virtual Conf. (2021).

[24]. Andreas Loren B, Jaudzems K, Stanek J, Lalli D, Bertarello A, Le Marchand T, Cala-De Paepe D, Kotelovica S, Akopjana I, Knott B, Wegner S, Engelke F, Lesage A, Emsley L, Tars K, Herrmann T, and Pintacuda G, "Structure of fully protonated proteins by proton-detected magic-angle spinning NMR", Proceedings of the National Academy of Sciences 113 (2016) 9187–9192.

[25]. Bahri S, Silvers R, Michael B, Jaudzems K, Lalli D, Casano G, Ouari O, Lesage A, Pintacuda G, Linse S, and Griffin Robert G, "1H detection and dynamic nuclear polarization–enhanced NMR of Aβ1-42 fibrils", Proceedings of the National Academy of Sciences 119 (2022) e2114413119.

[26]. Struppe J, Quinn CM, Lu M, Wang M, Hou G, Lu X, Kraus J, Andreas LB, Stanek J, Lalli D, Lesage A, Pintacuda G, Maas W, Gronenborn AM, Polenova T, Expanding the horizons for structural analysis of fully protonated protein assemblies by NMR spectroscopy at MAS frequencies above 100 kHz, Solid State Nucl. Magn. Reson 87 (2017) 117–125. [PubMed: 28732673]

[27]. Böckmann A, Ernst M, Meier BH, Spinning proteins, the faster, the better?, J Magn. Reson 253 (2015) 71–79. [PubMed: 25797006]

[28]. Penzel S, Oss A, Org M-L, Samoson A, Böckmann A, Ernst M, Meier BH, Spinning faster: protein NMR at MAS frequencies up to 126 kHz, J. Biomol. NMR 73 (2019) 19–29. [PubMed: 30680507]

[29]. Xue K, Sarkar R, Motz C, Asami S, Decker V, Wegner S, Tosner Z, Reif B, Magic-angle spinning frequencies beyond 300 kHz are necessary to yield maximum sensitivity in selectively methyl protonated protein samples in solid-state NMR, J. Phys. Chem. C 122 (2018) 16437–16442.

[30]. Abragam A, Goldman M, Principles of dynamic nuclear polarization, Rep. Prog. Phys 41 (1978) 395–467.

[31]. Overhauser AW, Polarization of nuclei in metals, Phys. Rev 92 (1953) 411–415.

[32]. Becerra LR, Gerfen GJ, Temkin RJ, Singel DJ, Griffin RG, Dynamic nuclear polarization with a cyclotron resonance maser at 5 T, Phys. Rev. Lett 71 (1993) 3561–3564. [PubMed: 10055008]

[33]. Hall DA, Maus DC, Gerfen GJ, Inati SJ, Becerra LR, Dahlquist FW, Griffin RG, Polarization-enhanced NMR spectroscopy of biomolecules in frozen solution, Science 276 (1997) 930–932. [PubMed: 9139651]

[34]. Jaudzems K, Bertarello A, Chaudhari SR, Pica A, Cala-De Paepe D, Barbet-Massin E, Pell AJ, Akopjana I, Kotelovica S, Gajan D, Ouari O, Tars K, Pintacuda G, Lesage A, Dynamic nuclear polarization-enhanced biomolecular NMR spectroscopy at high magnetic field with fast magic-angle spinning, Angew. Chem. Int. Ed 57 (2018) 7458–7462.

[35]. Berruyer P, Björgvinsdóttir S, Bertarello A, Stevanato G, Rao Y, Karthikeyan G, Casano G, Ouari O, Lelli M, Reiter C, Engelke F, Emsley L, Dynamic nuclear polarization enhancement of 200 at 21.15 T enabled by 65 kHz magic angle spinning, J. Phys. Chem. Lett 11 (2020) 8386–8391. [PubMed: 32960059]

[36]. Judge PT, Sesti EL, Saliba EP, Alaniva N, Halbritter T, Sigurdsson ST, Barnes AB, Sensitivity analysis of magic angle spinning dynamic nuclear polarization below 6 K, J. Magn. Reson 305 (2019) 51–57. [PubMed: 31212198]

[37]. Mathies G, Caporini MA, Michaelis VK, Liu Y, Hu K-N, Mance D, Zweier JL, Rosay M, Baldus M, Griffin RG, Efficient dynamic nuclear polarization at 800 MHz/527 GHz with Trityl-Nitroxide Biradicals, Angew. Chem. Int. Ed 54 (2015) 11770–11774.

[38]. Nanni EA, Barnes AB, Matsuki Y, Woskov PP, Corzilius B, Griffin RG, Temkin RJ, Microwave field distribution in a magic angle spinning dynamic nuclear polarization NMR probe, J. Magn. Reson 210 (2011) 16–23. [PubMed: 21382733]

[39]. Purea A, Reiter C, Dimitriadis AI, de Rijk E, Aussenac F, Sergeyev I, Rosay M, Engelke F, Improved waveguide coupling for 1.3 mm MAS DNP probes at 263 GHz, J. Magn. Reson 302 (2019) 43–49. [PubMed: 30953925]

[40]. Rosay M, Tometich L, Pawsey S, Bader R, Schauwecker R, Blank M, Borchard PM, Cauffman SR, Felch KL, Weber RT, Temkin RJ, Griffin RG, Maas WE, Solid-state dynamic nuclear polarization at 263 GHz: spectrometer design and experimental results, PCCP 12 (2010) 5850–5860. [PubMed: 20449524]

[41]. Thurber K, Tycko R, Low-temperature dynamic nuclear polarization with helium-cooled samples and nitrogen-driven magic-angle spinning, J. Magn. Reson 264 (2016) 99–106. [PubMed: 26920835]

[42]. Can TV, McKay JE, Weber RT, Yang C, Dubroca T, van Tol J, Hill S, Griffin RG, Frequency-swept integrated and stretched solid effect dynamic nuclear polarization, J. Phys. Chem. Lett 9 (2018) 3187–3192. [PubMed: 29756781]

[43]. Can TV, Tan KO, Yang C, Weber RT, Griffin RG, Time domain DNP at 1.2 T, J. Magn. Reson 329 (2021).

[44]. Tan KO, Weber RT, Can TV, Griffin RG, Adiabatic Solid Effect, J. Phys. Chem. Lett 11 (2020) 3416–3421. [PubMed: 32282219]

[45]. Jensen JE, Tuttle WA, Stewart RB, Brechna H, and Prodell AG, Brookhaven National Laboratory selected cryogenic data notebook: Volume 1, Sections 1-9, United States, 1980

[46]. Burghartz S, Schulz B, Thermophysical properties of sapphire, AlN and MgAl2O4 down to 70 K, J. Nucl. Mater 212–215 (1994) 1065–1068.

[47]. Inyushkin AV, Taldenkov AN, Ralchenko VG, Bolshakov AP, Koliadin AV, Katrusha AN, Thermal conductivity of high purity synthetic single crystal diamonds, Phys. Rev. B 97 (2018).

[48]. Yang H-S, Bai GR, Thompson LJ, Eastman JA, Interfacial thermal resistance in nanocrystalline yttria-stabilized zirconia, Acta Mater. 50 (2002) 2309–2317.

[49]. Naftaly M, and Miles RE, “Terahertz Time-Domain Spectroscopy for Material Characterization”, Proceedings of the IEEE 95 (2007) 1658–1665.

[50]. Barbet-Massin E, Pell AJ, Retel JS, Andreas LB, Jaudzems K, Franks WT, Nieuwkoop AJ, Hiller M, Higman V, Guerry P, Bertarello A, Knight MJ, Felletti M, Le Marchand T, Kotelovica S, Akopjana I, Tars K, Stoppini M, Bellotti V, Bolognesi M, Ricagno S, Chou JJ, Griffin RG, Oschkinat H, Lesage A, Emsley L, Herrmann T, Pintacuda G, Rapid proton-detected NMR assignment for proteins with fast magic angle spinning, J. Am. Chem. Soc 136 (2014) 12489–12497. [PubMed: 25102442]

[51]. Lewandowski JR, Sein J, Blackledge M, Emsley L, Anisotropic collective motion contributes to nuclear spin relaxation in crystalline proteins, J. Am. Chem. Soc 132 (2010) 1246–1248. [PubMed: 19916496]

[52]. Shaka AJ, Keeler J, Frenkiel T, Freeman R, An improved sequence for broadband decoupling: WALTZ-16, J. Magn. Reson 52 (1983) (1969) 335–338.

[53]. Zhou DH, Rienstra CM, High-performance solvent suppression for proton detected solid-state NMR, J. Magn. Reson 192 (2008) 167–172. [PubMed: 18276175]

[54]. Hermani J, Emonts M, and Brecher C, Nanosecond Laser Processing of Diamond Materials, Proceedings of the Lasers in Manufacturing Conference, Munich, Germany, 2015, pp. 22–25.

[55]. Konov VI, Laser in micro and nanoprocessing of diamond materials, Laser Photonics Rev. 6 (2012) 739–766.

[56]. Mouhamadali F, Equis S, Saeidi F, Best JP, Cantoni M, Hoffmann P, Wasmer K, Nanosecond pulsed laser-processing of CVD diamond, Opt. Lasers Eng 126 (2020).

[57]. Patil P, Laser direct-write fabrication of MEMS, Massachusetts Institute of Technology, 2019.

[58]. Ramaswamy C, Raman effect in diamond, Nature 125 (1930) 704.

[59]. Nemanich RJ, Solin SA, First- and second-order Raman scattering from finite-size crystals of graphite, Phys. Rev. B 20 (1979) 392–401.

[60]. Howe JY, The oxidation of diamond, Alfred University, 2001.

[61]. Paci JT, Minton TK, Schatz GC, Hyperthermal oxidation of graphite and diamond, Acc. Chem. Res 45 (2012) 1973–1981. [PubMed: 22694904]

[62]. Samoson A, H-MAS, J. Magn. Reson 306 (2019) 167–172. [PubMed: 31331763]

[63]. Wilhelm D, Purea A, Engelke F, Fluid flow dynamics in MAS systems, J. Magn. Reson 257 (2015) 51–63. [PubMed: 26073599]

[64]. Bouleau E, Lee D, Saint-Bonnet P, Hediger S, De Paëpe G, Ultra-low temperature nuclear magnetic resonance, IOP Conf. Ser.: Mater. Sci. Eng 171 (2017).

[65]. Matsuki Y, Nakamura S, Fukui S, Suematsu H, Fujiwara T, Closed-cycle cold helium magic-angle spinning for sensitivity-enhanced multi-dimensional solid-state NMR, J. Magn. Reson 259 (2015) 76–81. [PubMed: 26302269]

[66]. Myhre PC, Webb GG, Yannoni CS, Magic angle spinning nuclear magnetic resonance near liquid-helium temperatures. variable-temperature CPMAS studies of C4H7+ to 5 K, J. Am. Chem. Soc 112 (1990) 8992–8994.

[67]. Thurber KR, and Tycko R, "Biomolecular solid state NMR with magic-angle spinning at 25K", Journal of magnetic resonance (San Diego, Calif. : 1997) 195 (2008) 179–186 [PubMed: 18922715]

[68]. Herzog N, Weber A, Purea A, Osen D, Knott B, Engelke F, Wilhelm D, Ultra low temperature microturbine for magic angle spinning system, J. Fluids Eng 144 (2022).

[69]. Sesti EL, Alaniva N, Rand PW, Choi EJ, Albert BJ, Saliba EP, Scott FJ, Barnes AB, Magic angle spinning NMR below 6 K with a computational fluid dynamics analysis of fluid flow and temperature gradients, J. Magn. Reson 286 (2018) 1–9. [PubMed: 29161649]

[70]. Deb R, Hunkeler A, Wilhelm D, Jenny P, Meier BH, Numerical modeling and design decisions for aerostatic bearings with relatively large nozzle sizes in Magic-Angle Spinning (MAS) systems, Tribol. Int 175 (2022).

[71]. Endo Y, Hioka K, Yamauchi K, Sample Tube and Measurement Method for Solid State NMR, in: U.S.P. Office (Ed.), JEOL Ltd, United States, 2011, pp. 1–11.

[72]. Genta G., Dynamics of Rotating Systems, Springer, New York, 2005.

[73]. Drory MD, Dauskardt RH, Kant A, Ritchie RO, Fracture of synthetic diamond, J. Appl. Phys 78 (1995) 3083–3088.

[74]. Launey ME, Ritchie RO, On the fracture toughness of advanced materials, Adv. Mater 21 (2009) 2103–2110.

[75]. Liu X, Athanasiou CE, Padture NP, Sheldon BW, Gao H, A machine learning approach to fracture mechanics problems, Acta Mater. 190 (2020) 105–112.

[76]. Blauel JG, Beinert J, Wenk M, Fracture-mechanics investigations of cracks in rotating disks, Exp. Mech 17 (1977) 106–112.

[77]. Kulyk V, Duriagina Z, Kostryzhev A, Vasyliv B, Vavrukh V, Marenych O, The effect of Yttria content on microstructure, strength, and fracture behavior of Yttria-stabilized Zirconia, Materials (2022).

[78]. Marinis A, Aquilino SA, Lund PS, Gratton DG, Stanford CM, Diaz-Arnold AM, Qian F, Fracture toughness of yttria-stabilized zirconia sintered in conventional and microwave ovens, J. Prosthet. Dent 109 (2013) 165–171. [PubMed: 23522365]

[79]. Roitero E, Reveron H, Gremillard L, Garnier V, Ritzberger C, Chevalier J, Ultra-fine Yttria-Stabilized Zirconia for dental applications: a step forward in the quest towards strong, translucent and aging resistant dental restorations, J. Eur. Ceram. Soc (2022).

[80]. S.G. ZIRPRO, UprYZe-Shock Technical Data Sheet, 2020.

[81]. Liang Q, Yan C-S, Meng Y, Lai J, Krasnicki S, Mao H-K, Hemley RJ, Enhancing the mechanical properties of single-crystal CVD diamond, J. Phys. Condens. Matter 21 (2009).

[82]. Athanasiou CE, Liu X, Zhang B, Cai T, Ramirez C, Padture NP, Lou J, Sheldon BW, Gao H, Integrated simulation, machine learning, and experimental approach to characterizing fracture instability in indentation pillar-splitting of materials, J. Mech. Phys. Solids 170 (2023).

[83]. Athanasiou C-E, and Bellouard Y, A Monolithic Micro-Tensile Tester for Investigating Silicon Dioxide Polymorph Micromechanics, Fabricated and Operated Using a Femtosecond Laser, Micromachines, 2015, pp. 1365–1386

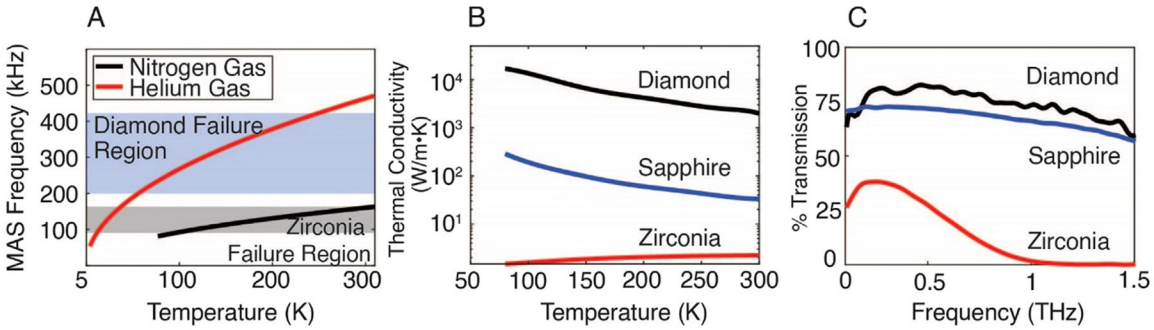

Fig. 1.

Advantages of diamond rotors. (A). The diamond mechanical failure region is estimated to be a factor of 1.5–2.5 times higher than that of conventional YSZ rotors. Over the range of required temperatures for DNP NMR, using diamond will allow for MAS frequency increase by taking advantage of helium gas's high speed of sound. Speed of sound data for both helium and nitrogen gases as a function of temperature were obtained from Ref [45]. (B). The improved thermal conductivity of single crystal diamond relative to sapphire or zirconia offers rapid sample temperature equilibration and efficient heat dissipation induced during at high spinning frequencies and microwave irradiation under DNP. Thermal conductivity data obtained from Ref [46-48]. (C). THz field transmission measurement for diamond, sapphire ('C-cut' orientation), and zirconia.

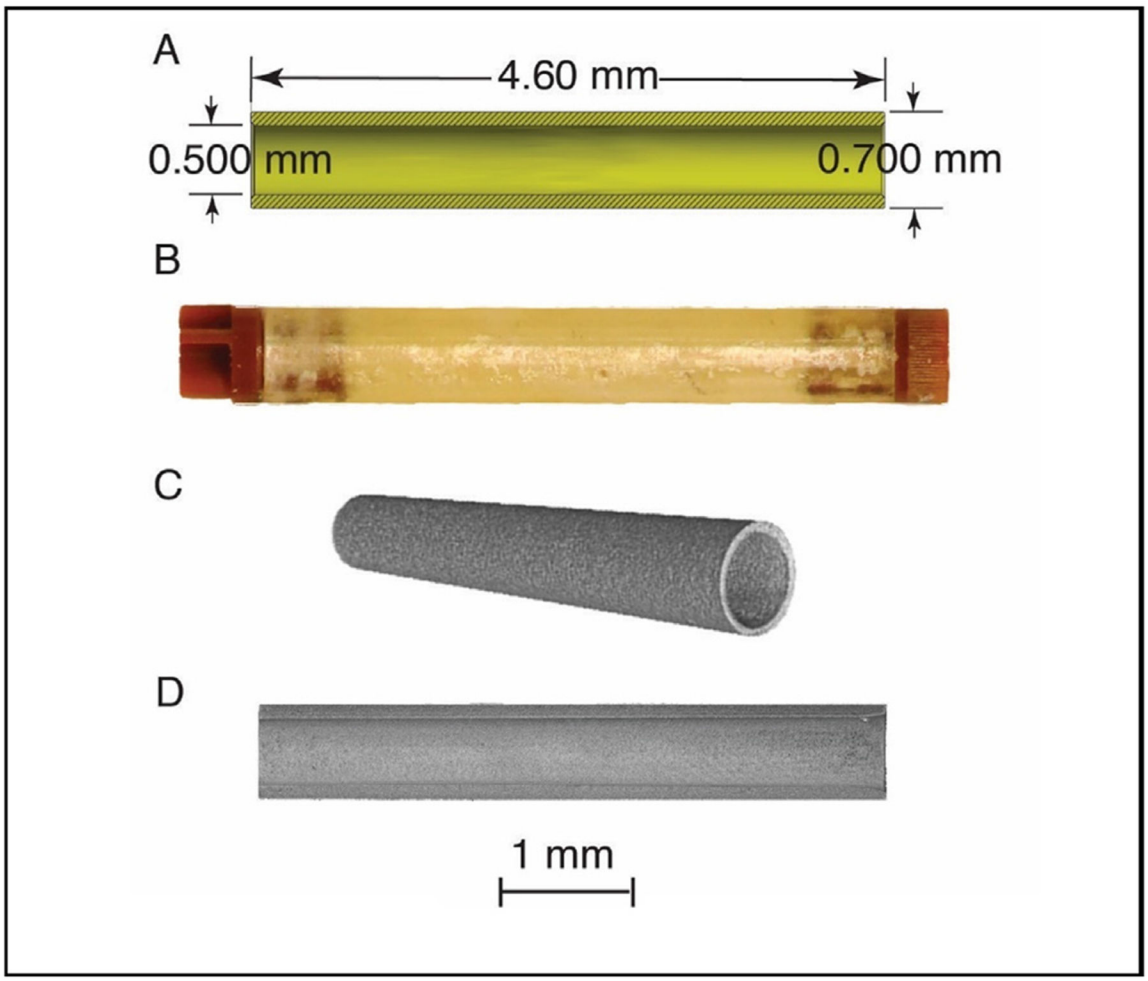

Fig. 2. Diamond rotors.

(A). CAD model of 0.7 mm rotor and associated dimensions. (B). Photograph of assembled diamond rotor including drive tip and end cap. (C). Isometric view of diamond rotor from a microCT scan. (D). Cross section view of a microCT scan of a diamond rotor.

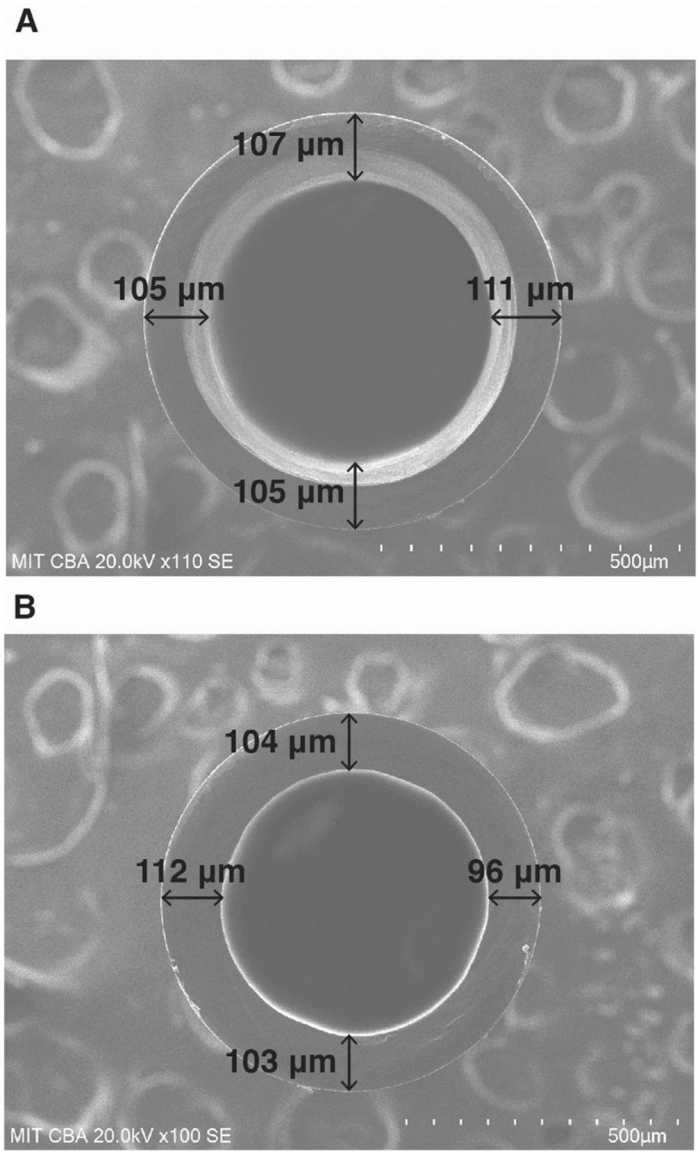

Fig. 3. Scanning electron microscopy of diamond rotor.

(A). Diamond rotor side 1 with annotated wall thickness. (B). Diamond rotor side 2.

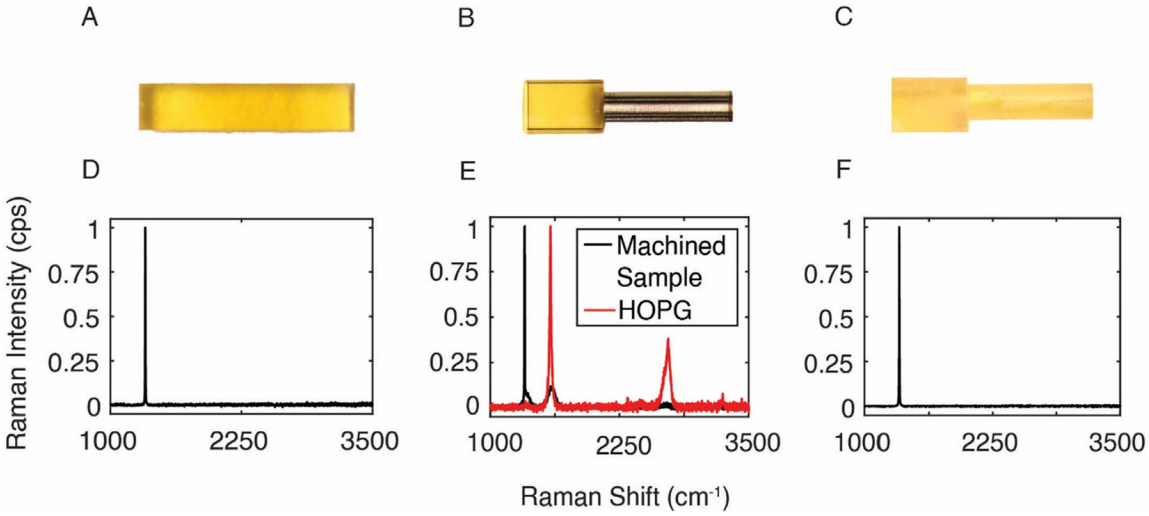

Fig. 4. Raman analysis of diamond rotor fabrication.

(A, D). In the starting material only diamond is detected. (B). Photograph of machined diamond material without heat treatment; graphite layer is visually contrasted with unmachined yellow diamond. (C). After heat treatment the graphite is observed to be removed. (E). Raman spectroscopy of HOPG graphite Raman spectra (red) used as a standard sample used to confirm presence of graphite on machined sample (black). (F). Following 24-hour heat treatment, graphite is removed from the machined sample.

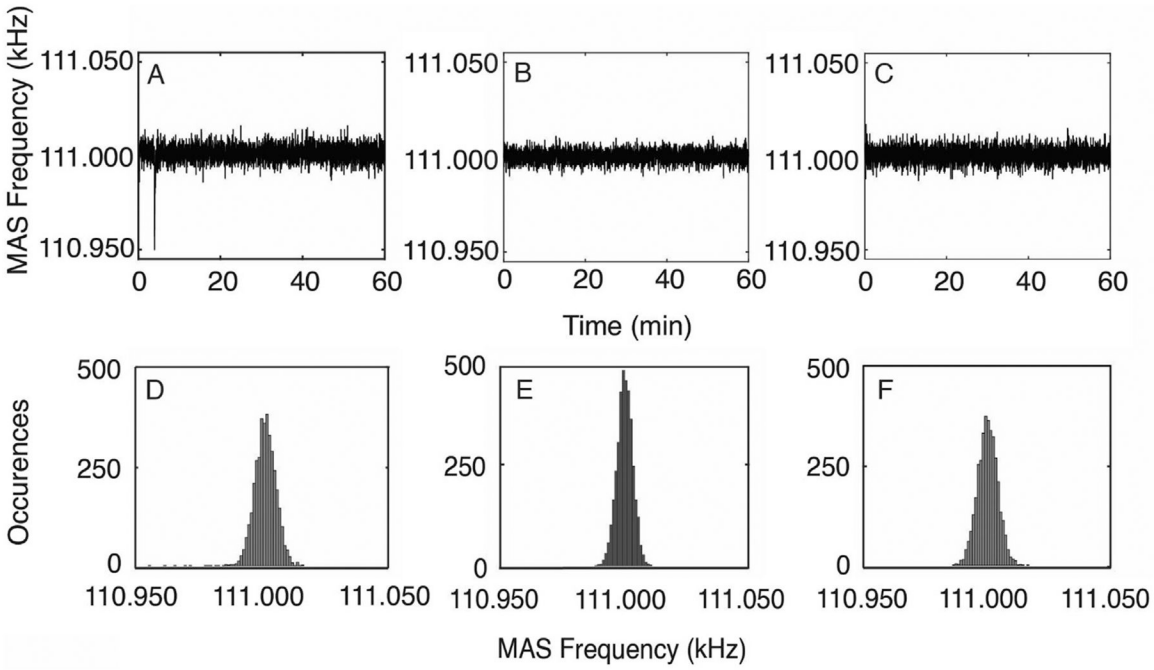

Fig. 5. MAS stability measurements.

Top Row shows time dependent traces of (A) YSZ rotor. (B). Diamond rotor 1. (C). Diamond rotor 2. Bottom row shows histogram plot at a mean spinning frequency of 111.001 kHz (D) YSZ rotor, standard deviation of 4.43 Hz (E). Diamond rotor 1, standard deviation of 3.13 Hz. (F). Diamond rotor 2, standard deviation of 4.04 Hz.

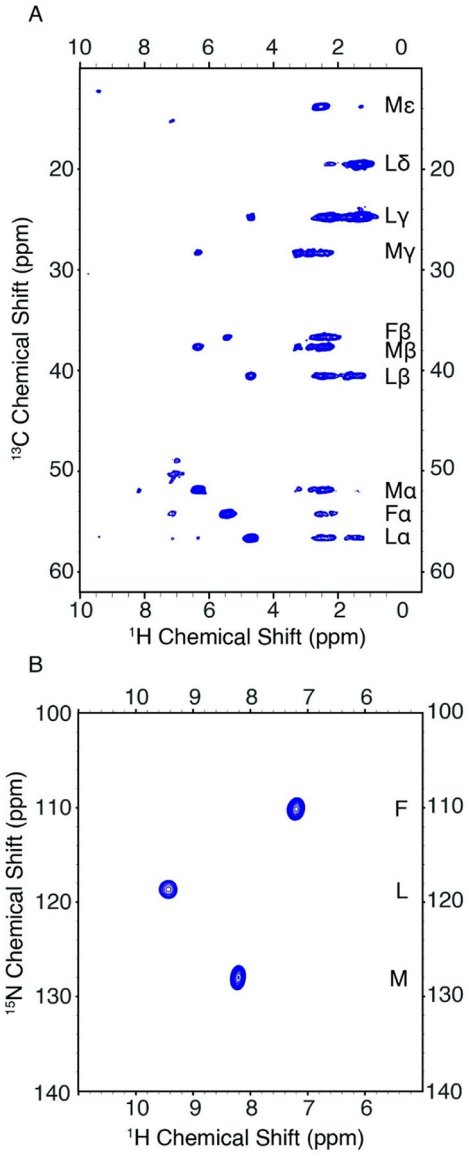

Fig. 6. ^{1}H detected spectra of U-^{15}N,^{13}C-N-*f*-MLF-OH recorded using a diamond rotor.
(A). (H)CH correlation spectrum. (B). (H)NH correlation spectrum.

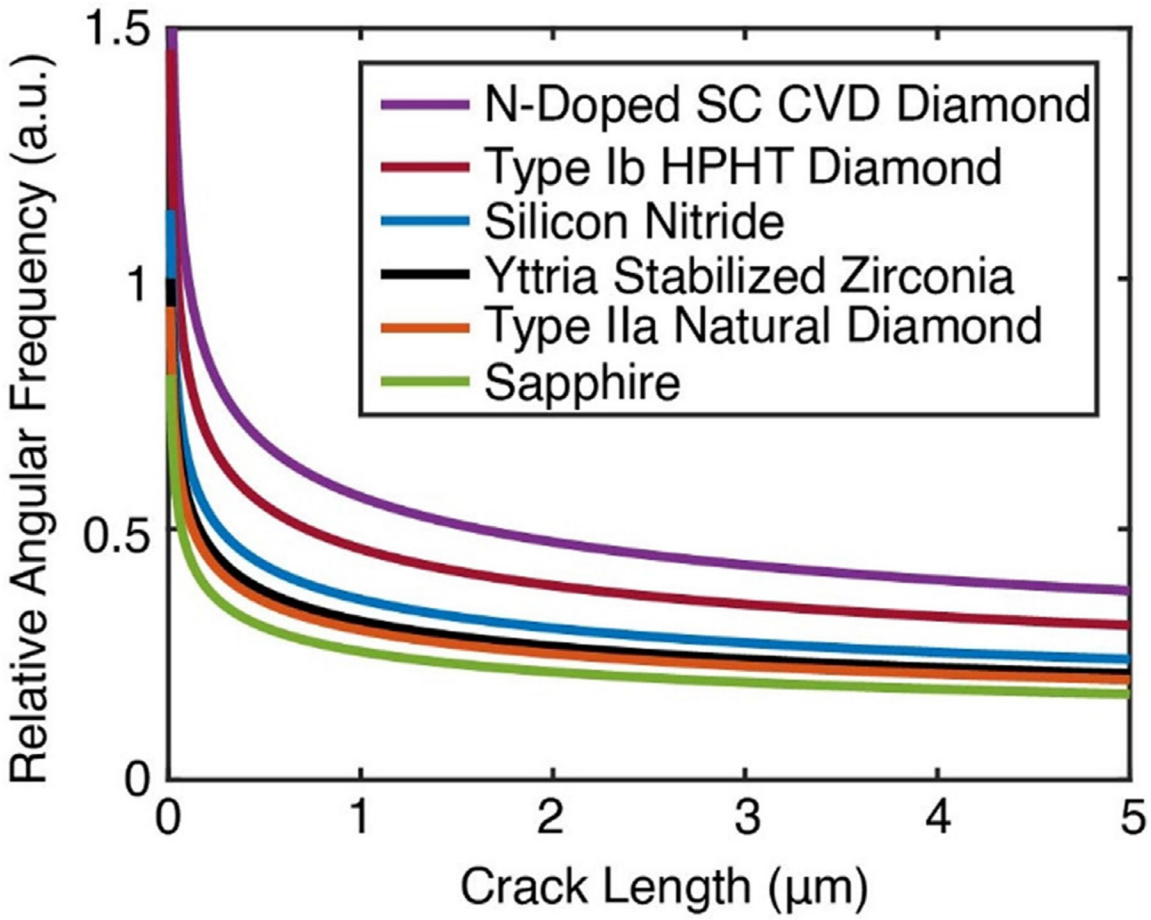

Fig. 7.
Fracture mechanics derived relative angular frequencies. All angular frequencies are relative to YSZ.